Chemical Engineering Journal 396 (2020) 125161

Contents lists available at ScienceDirect

Chemical Engineering Journal

journal homepage: www.elsevier.com/locate/cej

$LaCl_3$ flux mediated Ta_3N_5 planar photoanode for solar water oxidation

Zirui Lou, Yingchen Yang, Yichen Wang, Chao Qin, Rong Liang, Yanwen Wang, Zhizhen Ye, Liping Zhu*

State Key Laboratory of Silicon Materials, School of Materials Science & Engineering, Zhejiang University, Hangzhou 310027, PR China

HIGHLIGHTS

- Efficient low-dose $LaCl_3$ flux mediated Ta_3N_5 photoanode was fabricated.
- High photoresponse of 8.2 mA cm^{-2} @ 1.23 V_{RHE} for La-Ta_3N_5 was achieved.
- DFT study reveals interfacial charge transfer and carrier concentration increase.

GRAPHICAL ABSTRACT

In this study, efficient Ta_3N_5 photoanode is fabricated on Ta foil by direct oxidation and nitridation method with $LaCl_3$ flux mediated treatment, the introduction of $LaCl_3$ flux brings a new look to this traditional method and it may potentially be applied to large area and low cost photoanodes.

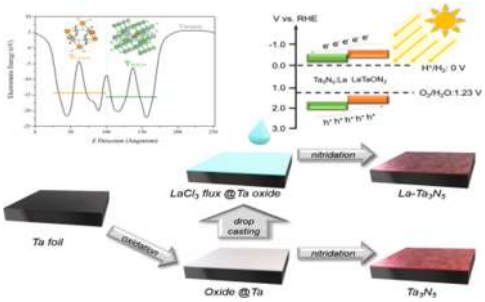

ARTICLE INFO

Keywords:
Lanthanum
Ta_3N_5
Photoanode
Doping
Heterostructure

ABSTRACT

Ta_3N_5 is a promising candidate for photoelectrochemical (PEC) water splitting. Recently gratifying photocurrents have been reported through various advanced techniques. However, obtaining high performance Ta_3N_5 photoanode prepared by direct oxidation and nitridation remains challenging. In this work, efficient Ta_3N_5 photoanode was fabricated on Ta foil by direct oxidation and nitridation method with $LaCl_3$ flux mediated treatment. The highest photoresponse (8.2 mA cm^{-2} @ 1.23 V_{RHE}) for direct oxidized and nitrided Ta_3N_5 is achieved with the help of $LaCl_3$ flux, which is nearly doubled compared to the untreated counterparts. Theoretical analysis suggests an interfacial charge transfer in $LaTaON_2/Ta_3N_5$ heterostructure and significant increase in carrier concentration on La doped Ta_3N_5 surface. The introduction of $LaCl_3$ flux brings a new look to this traditional method and it may potentially be applied to large area and low cost photoanodes.

1. Introduction

Photoelectrochemical (PEC) water splitting has attracted much attention as a strategy to convert solar energy into chemical energy in the form of hydrogen and oxygen, providing a feasible technical route for renewable energy [1]. Ta_3N_5, as a promising candidate, has attracted much attention among researchers due to its eligible band structure, adequate light absorption (~2.1 eV), low-cost and environmental friendliness [2–4]. However, defects and carrier recombination on surface/in bulk limit its performance [4–9].

In recent research, Ta_3N_5 photoanodes are mainly nitrided from anodized Ta_2O_5 nanotubes [10–14], deposited Ta_2O_5 nanorod [15,16], sputtering tantalum oxide [17,18] or alkali tantalate [19,20], and gratifying photocurrents have been obtained. However, there is few

* Corresponding author.
E-mail address: zlp1@zju.edu.cn (L. Zhu).

https://doi.org/10.1016/j.cej.2020.125161
Received 22 February 2020; Received in revised form 6 April 2020; Accepted 19 April 2020
Available online 23 April 2020
1385-8947/

breakthroughs in the traditional method of direct oxidation and nitridation of tantalum sheets. Zou et al. [21] pointed out that the passivation layer on the surface after nitridation would become carrier recombination centers and thermal or mechanical exfoliation can significantly improve photocurrent. Schmuki et al. [12] emphasize the beneficial effect of interfacial subnitrides on the photocurrent performance. Jaramillo et al. [22,23] proposed the formation mechanism of various types of subnitrides, and effect on charge transport of Ta_3N_5 by different film morphologies and thicknesses. Domen et al. [24,25] reported the conductivity of Ta_2N is better than Ta_5N_6 which favors charge transfer between Ta_3N_5 and back-electrode. Drawing on the experience of previous studies, we have got guiding ideology to overcome the shortcomings of traditional methods. However, obtaining high performance Ta_3N_5 photoanodes prepared by direct oxidation and nitridation remains challenging.

Doping and heterojunctions are two effective means to improve the photoelectrochemical performance [26–30]. Doping can effectively suppress oxygen defects in Ta_3N_5 by charge compensation [6,7,31], while heterojunction promotes the separation of photogenerated carriers (especially with its Ta-based perovskite oxynitride) through the driving force of energy level difference [32,33]. Combining these methods with the previous experience gives us inspiration.

Herein, we successfully obtained greatly enhanced PEC water splitting performance over a $LaCl_3$ flux mediated Ta_3N_5 planar photoanode prepared by a facile method directly oxidizing and nitriding with the assist of low-dose $LaCl_3$ flux. This electrode is compared with reference photoanode annealed in same process without $LaCl_3$ flux and each of them realized surface thermal exfoliation in order to reduce surface recombination sites. After co-catalyst deposition, we obtained 8.2 mA cm^{-2} and 4.2 mA cm^{-2} at 1.23 V_{RHE} for Ta_3N_5 photoanodes with/without the assist of $LaCl_3$ flux, respectively. Surface characterization of Ta_3N_5 demonstrate that nitriding with the assists of $LaCl_3$ flux results in better crystallization of the Ta_3N_5, the formation of $LaTaON_2$ and La doped Ta_3N_5 on the surface, which constructed better band alignment and simultaneously suppressed the carrier recombination on surface. Through the combination of experiment and theoretical calculation, we verify the mechanism of the enhancement of surface carrier concentration and photocurrent. Though this facile method is unable to obtain fine micro-nano structure, we can achieve competitive photoelectrochemical performance on $LaCl_3$ flux mediated Ta_3N_5 which can potentially be applied to large area and low cost photoanodes.

2. Experiment section

2.1. Chemicals

All the reagents were of analytical purity and were used without further purification. Cobalt acetate ($Co(CH_3COO)_2{\cdot}4H_2O$), ammonium hydroxide, methanol ethanol and acetone were purchased from Sinopharm. Lanthanum chloride ($LaCl_3{\cdot}7H_2O$) was bought from Aladdin. Deionized water was prepared using Millipore Milli-Q purification system (resistivity greater than 18 MΩ·cm).

2.2. Preparation of $LaCl_3$ flux mediated Ta_3N_5 photoanode

The Ta_3N_5 Planar Photoanode was synthesized through oxidation of Ta foil to form tantalum oxide and subsequent post-annealing in NH_3 to form tantalum nitride. For the oxidation procedure, Ta foil (0.2 mm thick, 99.95%, Zhongnuo Advanced Material) was first cut into 12 mm × 10 mm in size. The Ta foil was ultrasonicated in acetone, methanol, and deionized water respectively and then annealed in air at 500 °C for 1 h to form a grey oxide layer. Experiment for optimum oxidation temperature was presented in **Figs. S1 and S2**.

Before nitridation, $LaCl_3$ flux was operated as follow. Firstly, 0.5 M $LaCl_3$ methanol solution was prepared. Then the oxidized Ta foil was place on a 70 °C heating plate, follow by adding 100uL solution dropwise on the foil. As the solvent evaporated, it formed a dense, smooth and translucent $LaCl_3$ film. Experiment for optimum $LaCl_3$ concentration was presented in **Figs. S3 and S4**.

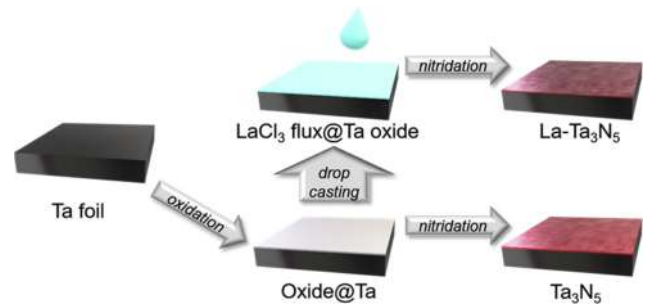

Fig. 1. Schematic illustration of the synthesis procedure of $LaCl_3$ flux mediated Ta_3N_5 planar photoanode.

The nitriding process was performed in a corundum-tube furnace. Prior to starting the nitriding process, applying a sufficient Ar flow to avoid oxygen is necessary. Then NH_3 flow (200 sccm) was controlled by a mass flow meter. The temperature was raised from room temperature to 900 °C at the rate of 10 °C min^{-1} and held at 900 °C for 5 hrs. After nitridation, redundant flux on the surface together with surface passivation layer can be easily peeled off and removed. $LaCl_3$ flux mediated Ta_3N_5 photoanode (named La-Ta_3N_5) was obtained after rinsing properly with deionized water and ethanol. The synthesis of Ta_3N_5 planar photoanode was similar to the process mentioned above but omitting the addition of $LaCl_3$ flux. The synthesis procedure is illustrated in Fig. 1.

2.3. Deposition of cocatalyst

Before the PEC measurements, Ta_3N_5 planar photoanode was modified with cobalt oxide (Co_3O_4) as co-catalyst, which was hydrothermally deposited onto Ta_3N_5 by a modified hydrothermal process [19,34]. Briefly, 10 mg $Co(CH_3COO)_2{\cdot}4H_2O$ was dissolved in 25.0 mL ethanol, followed by dropwise addition of 0.5 mL of 25% ammonium hydroxide under vigorous stirring. After stirring for 5 min, the solution was transferred into an autoclave. The Ta_3N_5 planar photoanode were immerged vertically with a PTFE holder in the solution. The autoclave was sealed and maintained at 120 °C for 1 h. After naturally cooled to room temperature, the electrodes were thoroughly washed with deionized water and ethanol then dried in air.

2.4. Characterization

The crystallographic structure of the as-prepared samples was investigated by the powder X-ray diffraction (PANalytical X'Pert PRO, operated at 40 kV and 40 mA with Cu Kα radiation (λ = 1.5406 Å)). The field emission scanning electron microscopy (SEM, Hitachi S-4800) and transmission electron microscopy (HR-TEM, FEI F20) equipped with energy dispersive X-ray spectroscopy (EDX) were used to identify the morphology and elemental compositions of the heterostructure. XPS spectra were recorded on a Kratos AXIS Supra spectrometer using a monochromatic Al Kα radiation source (1486.6 eV). The binding energies determined by XPS were calibrated with the adventitious carbon peak (284.8 eV) for each sample. UV–Vis diffuse reflectance spectra (DRS) were obtained using a Shimadzu UV-3600 spectrometer with $BaSO_4$ as a reference. Room-temperature photoluminescence (PL) measurements were carried out with excitation by a 405 nm laser to evaluate the optical property of the as-prepared samples.

2.5. Photoelectrochemical measurements

Photoelectrochemical measurements were carried out with a three-

electrode system in 1 M NaOH electrolyte (pH = 13.6). The photoelectrode was irradiated by a 300 W Xe lamp equipped with an AM 1.5G filter (PLS-SXE300, Beijing Perfectlight). And the intensity of simulated solar light (100 mW cm^{-2}) and monochromatic light obtained from bandpass filters was calibrated with an optical power and energy meter (Thorlabs). The Ag/AgCl reference potential was converted to reversible hydrogen electrode potential according to the Nernst relationship:

$$E(V_{RHE}) = E(V_{Ag/AgCl}) + 0.059 \times pH + 0.199$$

where 0.199 represents the standard potential of the KCl-saturated Ag/AgCl electrode at 25 °C.

The photocurrent was measured by linear sweep voltammetry with a scan rate of 10 mV s^{-1}. Chronoamperometry measurement was carried out at a potential of 1.23 V_{RHE} under AM 1.5 G illumination (100 mW cm^{-2}). Mott-Schottky (MS) analysis was carried out at 1500 and 1000 Hz and 15 mV amplitude under dark condition. In electrochemical impedance spectroscopy (EIS) measurements, Ta_3N_5 and a La-Ta_3N_5 were scanned at an AC amplitude of 10 mV with a frequency ranging from 100 kHz to 0.1 Hz. For IPCE measurements, we used the same instrument. The difference was that we used monochromatic irradiation from the Xe lamp equipped with bandpass filters (central wavelengths of 380 nm, 420 nm, 435 nm, 450 nm, 500 nm, 520 nm, 550 nm, 600 nm, 650 nm and 700 nm; band width of 20 nm). Then, the IPCE was calculated using the following equation: [35]

$$IPCE\% = \frac{1240(V \cdot nm) \times J(mA \cdot cm^{-2})}{P(mW \cdot cm^{-2}) \times \lambda(nm)} \times 100\%$$

In order to study the injection and separation efficiency of photoanode, we introduce electron donor as sacrificial agent, the electrolyte used was 0.2 M Na_2SO_3 solution, giving a final pH of 10.0. In NaOH electrolyte, the rate limiting step of photocurrent J_{NaOH} is the reaction of surface holes. After the sacrificial agent is introduced, the surface holes are quickly consumed due to the presence of electron donors. J_{Na2SO3} can be regarded as the maximum photocurrent of the as prepared material, and its limiting step became the carrier migration inside the material. Further improvement of material quality is needed to make it close to the theoretical photocurrent J_{abs}. Separation efficiency was calculated by J_{Na2SO3}/J_{abs}, while injection efficiency was calculated by J_{NaOH}/J_{Na2SO3}. The evolution of H_2 and O_2 was measured in 1 M NaOH solutions under AM 1.5 G illumination at 1.2 V_{RHE} on a Labsolar-III system (Beijing Perfectlight) equipped with a PEC reactor. Evolved H_2 and O_2 were analyzed online by gas chromatography (GC9790, Zhejiang Fuli) equipped with a thermal conduction detector, and Ar was used as carrier gas.

2.6. Computational method

Our DFT calculations were performed using the projected augmented wave (PAW) plane-wave basis in the Vienna *ab initio* simulation package (VASP) [36]. A plane-wave cutoff energy of 400 eV was employed. The generalized gradient approximation (GGA) proposed by Perdew, Burke, and Ernzerhof (PBE) is selected for the exchange–correlation potential [37]. The energy criterion is set to 10^{-5} eV in iterative solution of the Kohn-Sham equation. The k-points meshes for Brillouin zone integration is 8 × 3 × 3 and 4 × 4 × 6 for Ta_3N_5 and $LaTaON_2$ and La doping concentration for Ta_3N_5:La supercell is 1.04% (atomic ratio in the whole supercell). All the structures are relaxed until the residual forces on the atoms have declined to less than 0.03 eV/Å.

To simulate the La doped Ta_3N_5, a 3 × 1 × 1 Ta_3N_5 super-cell is built, which includes 60 N atoms, 35 Ta atoms and 1 center substituted La atom. When we use the super-cell, the band folding effect may exist in the band structure [7]. Thus, we enlarge the undoped Ta_3N_5 into a 3 × 1 × 1 super-cell to obtain similar structure and band number in order to better compare the electronic properties before and after doping. 4 × 1 and 5 × 1 supercell for Ta_3N_5 (1 1 0) and $LaTaON_2$ (2 0 0) planes are chosen to form heterostructure. The planar-averaged potential $\bar{V}$ across the interface was then obtained using the expression:

$$\bar{V}(z) = \frac{1}{S}\int_S V(\vec{r})dxdy$$

where S represents the area of a unit cell in the plane parallel to the interface (xy-plane).

The effective mass was calculated from the equation:

$$\frac{1}{m^*} = \frac{1}{\hbar^2}\frac{\partial^2 E(k)}{\partial k^2}$$

where $\hbar$ is the reduced Planck constant and m* is the effective mass. Thus, the effective mass follows from the second derivative of E with respect to the wave vector k.

3. Result and discussion

From the cross-section SEM image, Ta_3N_5 (Fig. 2**a**) and La-Ta_3N_5 (Fig. 2b) exhibited a planar photoanode with the nitride tightly adhered to the metal Ta substrate which enables adequate electrical conductivity, and the thickness was ca. 500 nm. Fig. 2c and 2d indicate the film have a rough surface morphology. After further comparison of the inset picture we can find subtle differences. Ta_3N_5 has a porous structure formed during the transition from Ta oxide to its nitride [23,38] and has a granular assembling morphology, while La-Ta_3N_5 has a relatively dense surface. It corresponds to the results from HRTEM image, we can find more holes in the grains of Ta_3N_5 (Fig. 2e), while the grains of La-Ta_3N_5 (Fig. 2f) are denser. The lattice fringes in the HRTEM images shows a well-defined crystalline structure with lattice spacings of 0.298 nm and 0.301 nm, corresponding to the value of (1 1 2) planes of the Ta_3N_5 phase. Further observations revealed that trace $LaTaON_2$ (0.286 nm (2 0 0) planes) can be identified on the surface of some Ta_3N_5 grains.

The crystallographic structure of the $LaCl_3$ flux mediated Ta_3N_5 (La-Ta_3N_5) and the bare Ta_3N_5 were determined by X-ray diffraction (XRD) analysis. As observed in Fig. 3, diffraction peaks of both La-Ta_3N_5 and bare Ta_3N_5 samples are well ascribed to Ta_3N_5 (PDF#79–1533) and Ta_2N (PDF#26-0985). Ta_2N is considered to be a conductive phase existed in the interlayer of Ta_3N_5/Ta and no other less conductive phase like Ta_4N_5 or Ta_5N_6 was probed, suggesting a better conductivity of the interlayer that favors carriers' migration.[24] The mechanism of the only Ta_2N may originate from the nitridation of suboxides at the Ta_2O_5/Ta interface into lower valence nitrides.[22] The grey colored oxide layer formed during partial oxidation in air contains suboxides. It is noteworthy in the enlarged view of XRD patterns around 31°, a weak peak accompany with the Ta_3N_5 (0 2 3) peak corresponds to the (2 0 0) peak of perovskite $LaTaON_2$ phase (PDF #53–0960) and a slight shift of diffraction peaks toward lower angles for La-Ta_3N_5, implying lattice expansion by La incorporation.

The PEC performances of bare Ta_3N_5 and La-Ta_3N_5 with/without Co_3O_4 co-catalyst loading (named Ta_3N_5-Co and La-Ta_3N_5-Co, respectively) were measured in 1 M NaOH electrolyte. As presented in Fig. 4**a**, without co-catalyst, the photocurrent density of bare Ta_3N_5 at 1.23 V_{RHE} is 0.8 mA cm^{-2}, which are comparable with the alkalinous performance of most existing reports on bare Ta_3N_5 [5,10,20,31]. Surprisingly, with the assist of $LaCl_3$ flux, the photocurrent has doubled to 1.7 mA cm^{-2}. Furthermore, after Co_3O_4 co-catalyst loading, 8.2 mA cm^{-2} and 4.2 mA cm^{-2} at 1.23 V_{RHE} was achieved for La-Ta_3N_5-Co and Ta_3N_5-Co photoanodes, respectively.

In Fig. 4b, the absorption edge of bare Ta_3N_5 is at 600 nm, while the absorption edge of La-Ta_3N_5 exhibits a relative red shift. According to previous reports, Ta_3N_5 is about 2.1 eV [39] and $LaTaON_2$ is about 1.9 eV [40,41]. This provides indirect evidence for the formation of $LaTaON_2$. IPCE action spectra show the quantum efficiency under different irradiation wavelengths, which are in agreement with the

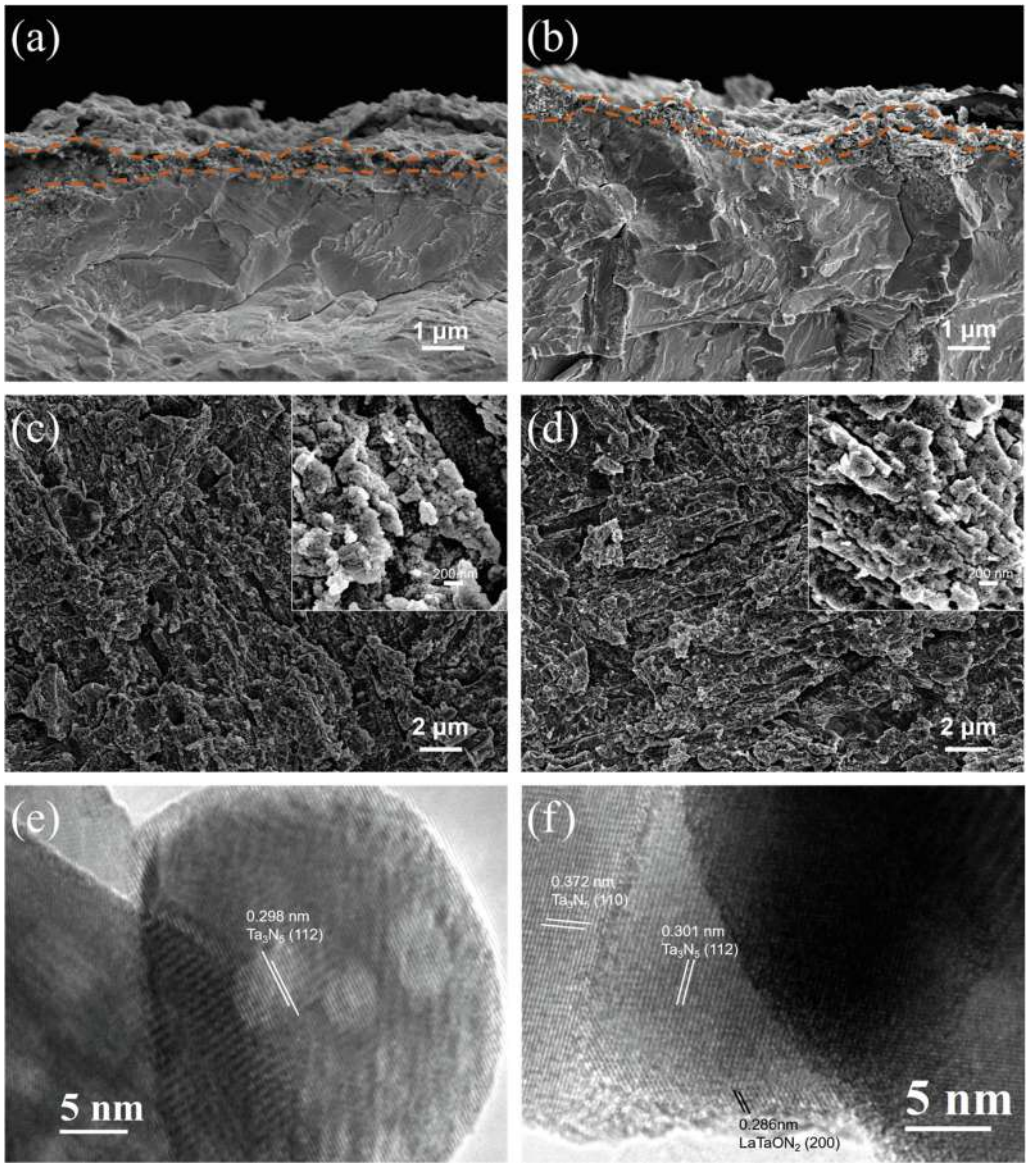

Fig. 2. SEM cross section view, top view, TEM image of (a)(c)(e) Ta_3N_5 and (b)(d)(f) La-Ta_3N_5, respectively. The orange dash line highlighted the thickness of the nitride layer.

absorption of Ta_3N_5. The IPCE is operated at 1.23 V_{RHE} after loading Co_3O_4 co-catalyst to promote the separation of photogenerated carriers. The bare Ta_3N_5-Co shows relatively low IPCE around 20%, however after the $LaCl_3$ flux treatment, the IPCE of La-Ta_3N_5-Co photoanode dramatically increases to more than 55%, even exceeds 60% at 500 nm.

Furthermore, chopped chronoamperometry measurement reveals the stabilities of the two photoanodes, as shown in Fig. 4c. For Ta_3N_5-Co, the photocurrent decreased rapidly, and corrosion may exist on the surface. For La-Ta_3N_5-Co, we also found a decrease in the photocurrent but slower than the bare sample. After 20 min test, the photocurrent of La-Ta_3N_5-Co is around 70% of its initial value, while that of Ta_3N_5-Co is reduced by half. Severer charge recombination is expected within bare Ta_3N_5 due to surface oxidation,[5] intrinsic oxygen impurity[7] and they affects the charge states.

Fig. 4d and 4e visualizes the enhanced charge transport efficiency in the bulk (separation efficiency) and surface (injection efficiency), respectively. J_{abs} and J_{Na2SO3} were shown in **Fig. S7**. The injection efficiency of La-Ta_3N_5-Co is greatly improved which indicating the charge transfer at the interface is unobstructed, it is one of the reasons for less photocurrent deterioration. The increase of separation efficiency of La-Ta_3N_5-Co may be due to surface doping and formation of heterojunction, which elevate the concentration of carriers and promote their separation. The increased charge injection and separation would suppress the charge recombination both at the interfaces and in bulks.

Then we will explore the mechanism of La element in photoelectrochemical performance enhancement. From the fine XPS spectrum of La 3d orbit (Fig. 5), the sample surface contains trace La element. In La 3d spectrum of La-Ta_3N_5, the peak position of the two small peaks (835.2 eV, 851.9 eV) and their binding energy difference (16.7 eV) conforms to the characteristics of La 3d orbit [42], thus we can confirm the existence of La element in La-Ta_3N_5 which is about 0.8% on the sample surface semiquantitatively. Based on the previous observations from XRD and TEM, we conclude that La is doped in Ta_3N_5 and in the form of a small amount of $LaTaON_2$ exists on La doped Ta_3N_5 surface. Next, we will use other methods to test this hypothesis.

Fig. 6**a** displays the Nyquist plot of EIS measured frequency range from 100 kHz to 0.1 Hz and the corresponding equivalent circuit diagram. R_s represents the series resistance of the photoanode, R_{bulk} and C_{bulk} represent the electron transport resistance and capacitance from Ta_3N_5 and its interface with Ta substrate, R_{ct} reflects the charge transfer

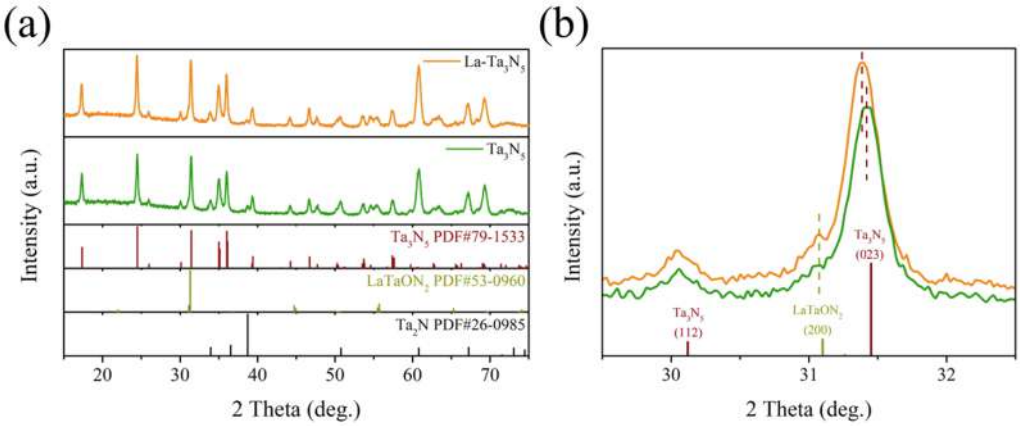

Fig. 3. (a) XRD patterns and (b) enlarge view of Ta_3N_5 and La-Ta_3N_5. The standard XRD pattern for Ta_3N_5 (PDF#79–1533), $LaTaON_2$ (PDF#53–0969) and Ta_2N (PDF#26–0985) was shown for reference.

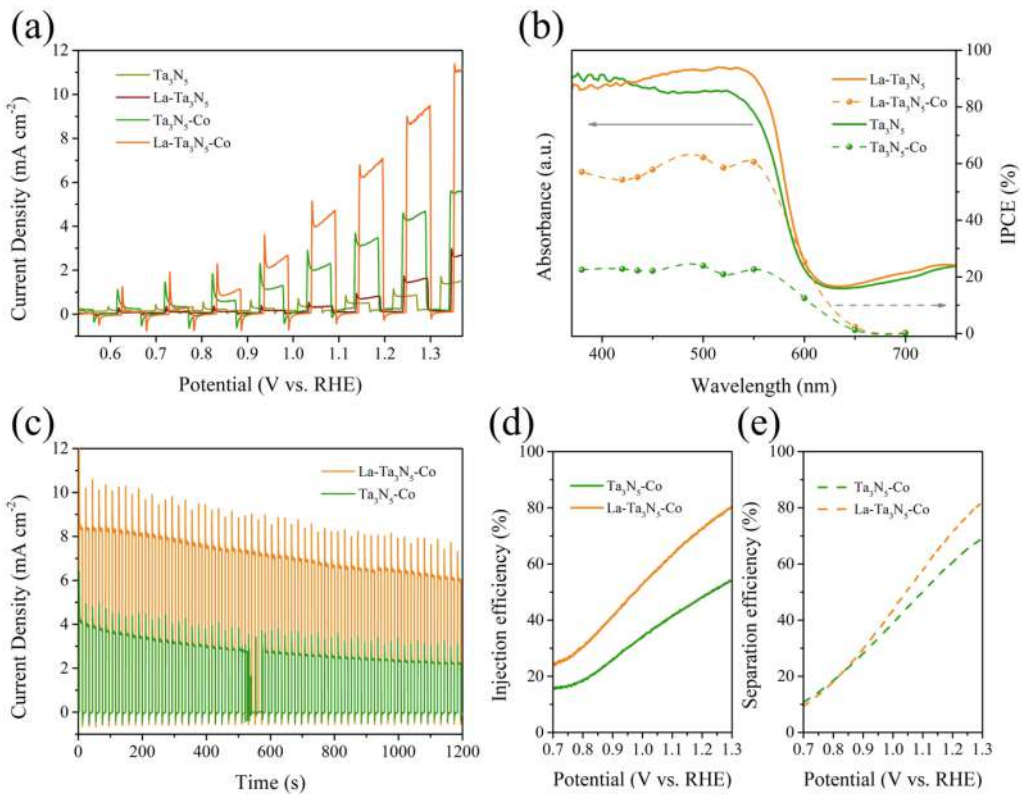

Fig. 4. (a) Current–potential curves with a scan rate of 10 mV s^{-1}, (b) UV–Vis absorption spectra and corresponding IPCE at 1.23 V_{RHE}, (c) time course photocurrent curves at 1.23 V_{RHE}, (d) injection efficiency and (e) separation efficiency of Ta_3N_5 and La-Ta_3N_5. Note that (a)(b)(c) were performed in 1 M NaOH (pH = 13.6), (d) (e) were performed in 0.2 M Na_2SO_3 (pH = 10) under AM1.5 irradiation (100 mW cm^{-2}).

resistance across the Ta_3N_5/electrolyte interface and C_{dl} is double layer capacitance [43]. It is noteworthy that in the inset diagram of high frequency region, the two samples show different characteristics. The intercept of the Z' axis reflects R_s of the system. La-Ta_3N_5 has a smaller R_s and R_{ct}, probably because surface La doping increases its carrier concentration and makes it more conductive. Compared with Ta_3N_5, La-Ta_3N_5 has a distinct superimposed smaller semicircle, which indicates there may be two different channels for electron transport in the photoanode. The formation of heterojunctions can significantly reduce R_{bulk} [33,44–46]. Therefore, we believe that this is due to the formation of $LaTaON_2$/Ta_3N_5 heterojunctions in some regions on the photoanode.

Photoluminescence (PL) spectra is generally held to demonstrate the separation efficiency of photo-induced carriers in the semiconductor since electron-hole pairs recombine to generate the PL emission signal [32,47]. Fig. 6b shows that PL signal decreases evidently in La-Ta_3N_5 which reflects the efficient separation of photo-excited electron-hole pairs. This may due to the suppression of O impurity level by surface La doping [7,8,48], and the formation of small amount of $LaTaON_2$ on the surface which forms heterojunction and promotes carrier separation.

The Mott-Schottky (MS) measurement was carried out under dark conditions to study the electronic properties. After linear fitting of the linear regions of the MS plots (Fig. 6c). We can get semiconductor type, carrier concentration and flat-band potential (E_{FB}) at the semiconductor/electrolyte interface from the slopes and interceptions of the fitting lines, the E_{FB} of the two samples were obtained, ~-0.12 V vs. RHE for Ta_3N_5 and ~ −0.18 V vs. RHE for the La-Ta_3N_5. For an n-type semiconductor under depletion condition, the relationship of polarization and capacitance can be described by MS equation [24,43,44].

$$\frac{1}{C_{SC}^2} = \frac{2}{\varepsilon_r \varepsilon_0 e N_D}\left[(E - E_{FB}) - \frac{kT}{e}\right]$$

where C_{SC}, ε_r, ε_0, N_D, E and E_{FB} are the space-charge capacitance,

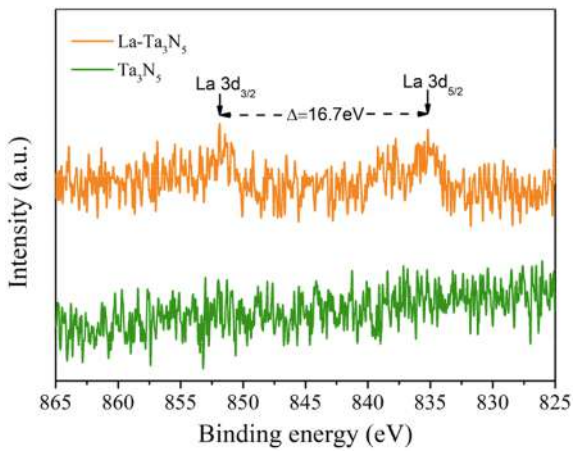

Fig. 5. XPS La 3d spectra of Ta_3N_5 and La-Ta_3N_5.

relative dielectric constant, vacuum permittivity (8.854×10^{-12}F m^{-1}), carrier concentration, applied potential and flat-band potential, respectively. It can be deduced from the formula that the slope (S) of linear fitting has such a relationship with $N_D = 2/(\varepsilon_r \varepsilon_0 e S)$. When taking $\varepsilon_r = 110$ for Ta_3N_5 into account [24], the carrier concentration of La-Ta_3N_5 is calculated to be 6.11×10^{19} cm^{-3} at the frequency of 1000 Hz, over one order of magnitude higher than 3.23×10^{18} cm^{-3} for Ta_3N_5.

XPS valence band scan suggests that energy gaps between the Fermi level (E_F) and the valence band maximum (VBM) are ~1.29 and ~1.48 eV for Ta_3N_5 and La-Ta_3N_5 respectively (Fig. 6d). The surface La doping makes the Fermi level increase slightly, which also confirms the increase of carrier concentration.

Based on the experimental data, we explain the mechanism of performance improvement through DFT calculation. The Ta_3N_5 crystal has an orthorhombic structure with space group *Cmcm*. The conventional unit cell consists of 32 atoms, where each Ta atom has six N atom neighbors, while N atoms have 3 or 4 Ta atom neighbors. Based on these computational parameters, the relaxed lattice constants of conventional Ta_3N_5 cell are a = 3.90, b = 10.26 and c = 10.27 Å, which agree within the experimental PDF card #79–1533 (a = 3.89, b = 10.21 and c = 10.26 Å). In the experiment, we have got the doping amount of La is about 0.8%. A conventional unit cell can't simulate the very small amount of dopant in Ta_3N_5. Thus, we choose a 3 × 1 × 1 Ta_3N_5 super-cell consists of 96 atoms where a substituted atom can provide about 1% doping concentration (atomic ratio in the whole supercell). The atomic structures were illustrated in Fig. 7**a and 7d**. As expected, the DFT/PBE band gaps are underestimated when compared to the experimental result, so we only analyze the relative value, not the absolute value. The Fermi surface (same as VBM) is set to 0 eV.

The bandstructures before and after doping were presented in Fig. 7b and 7e, respectively. We found that Ta_3N_5 is an indirect bandgap semiconductor with the VBM located between Y point and Γ point while the CBM located at Γ point. After La doping, the CBM, VBM and band gap remain unchanged, indicating that La doping does not form impurity level. However, most of bands became flatter. The wider the band, that is, the greater the fluctuation in the band structure, indicates that the smaller effective mass of electron in the band, the greater non localized. On the contrary, a flatter band indicates that the electron localization on this band is very strong and the effective mass is relatively large. We have calculated the effective mass at each CBM and VBM along opposite directions to get deep insight into the carrier transport properties of Ta_3N_5 and Ta_3N_5:La.

The effective masses of holes (m_h^*) and electrons(m_e^*) are taken from the second derivative fits of the bands. As presented in Table 1, after La doping, both m_h^* and m_e^* are increased obviously. This suggests that Ta_3N_5:La may have lower carrier mobilities and result in poor charge

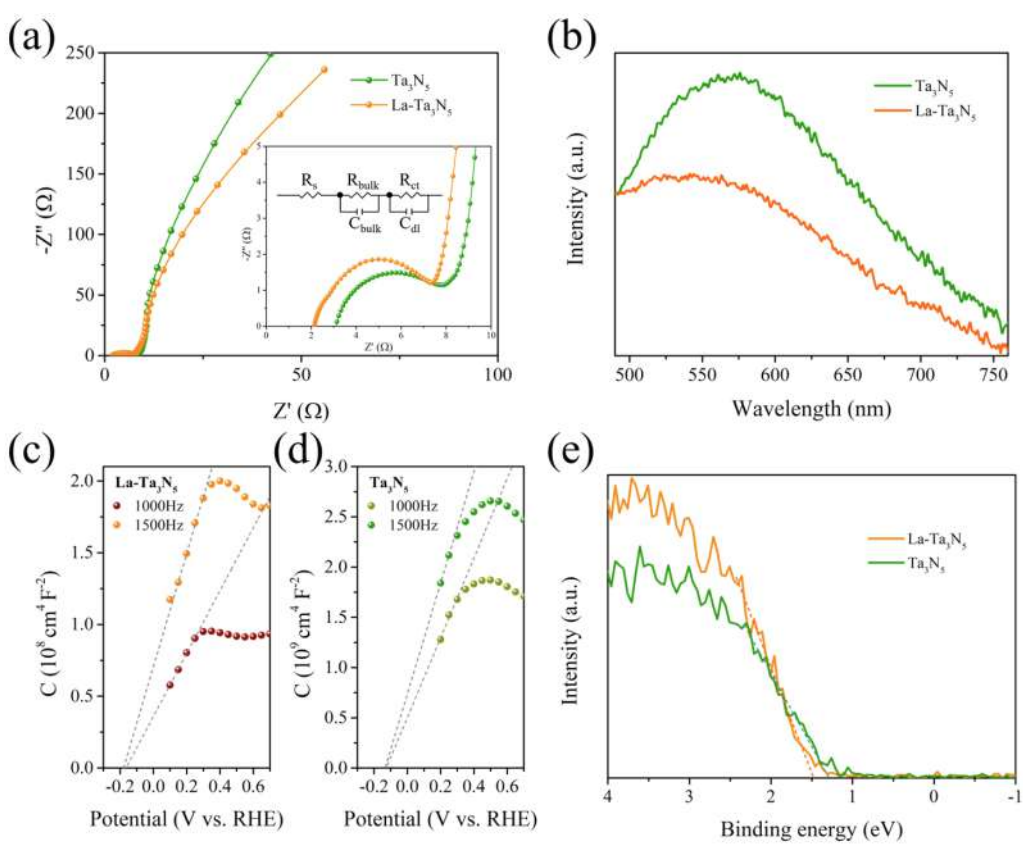

Fig. 6. (a) Nyquist plots from EIS measurement, (b) room-temperature PL spectra, (c)(d) Mott–Schottky plots, (e) XPS VBM spectra of Ta_3N_5 and La-Ta_3N_5.

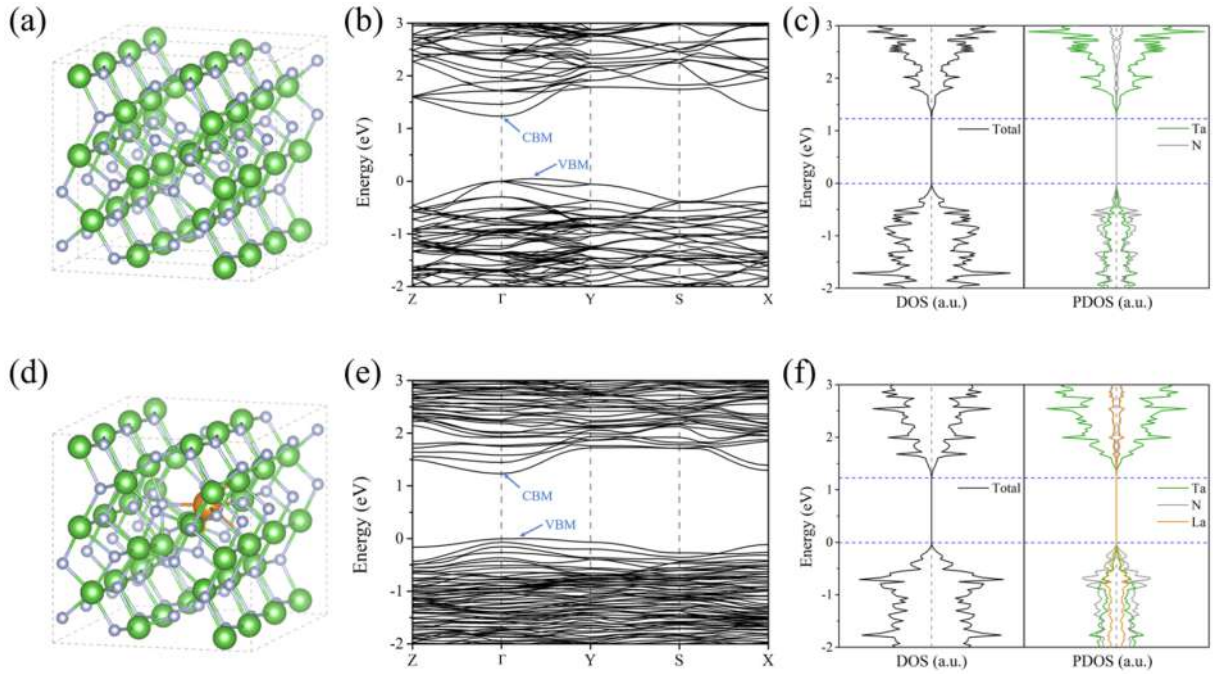

Fig. 7. Structure, band structure, density of state of (a)(b)(c) Ta_3N_5 and (d)(e)(f) Ta_3N_5:La, respectively. La, Ta, N atoms are shown in orange, green and grey.

Table 1
Effective masses of electron and hole in undoped Ta_3N_5 and La doped Ta_3N_5 along different directions.

	m_e^*		m_h^*	
	CBM → Z	CBM → Y	VBM→Γ	VBM → Y
Ta_3N_5	0.666	0.185	0.767	0.957
Ta_3N_5:La	0.730	0.231	1.623	0.915

transport properties. However, the energy band of Ta_3N_5:La is denser near Fermi level. It can be inferred that La doping is not suitable for bulk doping and the sample can not be too thick.

The density of states (DOS) and partial density of states (PDOS) displayed in Fig. 7c shows that in undoped Ta_3N_5 the top of the valence band is mainly composed of N 2p orbitals, while the bottom of the conduction band is mainly composed of Ta 5d orbitals. After La doping (Fig. 7f), La 5d contributes little to the bottom of the conduction band but has more significant effect on the top of valence band than Ta 5d. The DOS at the top of the valence band near the Fermi level is greatly increased, thus the corresponding carrier concentration is expected to be increased. This result suggests an increase of carrier concentration in Ta_3N_5:La that causes Fermi level to become lifted, which is consistent with the XPS VBM results.

In the experiment, we found the existence of $LaTaON_2/Ta_3N_5$:La heterostructure. Investigating the interfacial properties of trace nano-heterostructures experimentally was difficult due to the small size and amount of samples. However, theoretical calculations methods did not face these problems and could help us to deeply understand the charge transfer process on the interface. We build a theoretical model of $LaTaON_2/Ta_3N_5$:La as shown in Fig. 8**a**. The Ta_3N_5 (1 1 0) facet and $LaTaON_2$ (2 0 0) facet has a higher exposure rate according to the TEM and XRD results. Considering the in-plane lattice constant of Ta_3N_5 (1 1 0) and $LaTaON_2$ (2 0 0) are 10.26/5.48 Å and 8.06/5.71 Å, respectively. And the in-plane angles are both 90°. We, therefore, chose 4 × 1 and 5 × 1 supercell for Ta_3N_5 (1 1 0) and $LaTaON_2$ (2 0 0) planes to form heterostructure in order to minimize lattice mismatch. Similarly, we substitute a Ta atom with La atom on the surface of Ta_3N_5 side to achieve a surface doping concentration of about 1%.

The corresponding electrostatic potentials obtained for $LaTaON_2$ (2 0 0)/ Ta_3N_5:La (1 1 0) interface was plotted in Fig. 8b. As illustrated, the corresponding averaged potential $\bar{V}$ variation along the direction perpendicular to the interface shows that the Ta_3N_5:La plane are located in more negative potential regions than the $LaTaON_2$ plane, suggesting that electrons in $LaTaON_2$ have a trend of transfer to Ta_3N_5:La side. The electrostatic potentials revealed that the lower positive potential was located at the contact interface, which means no barrier for carrier transport at the contact interface. And the unobstructed migration channel should be caused by the lattice and electrons match at the interface of Ta_3N_5 and $LaTaON_2$. The surface doping of La may acts as a bridge to transfer carriers at the interface. Thus, the charge density difference of $LaTaON_2$ (2 0 0)/Ta_3N_5:La (1 1 0) heterostructure was calculated to confirm the above carrier transfer behavior (Fig. 8c). It is obviously that charge depletion (cyan region) occurs around the Ta and La atoms on $LaTaON_2$ plane while charge accumulation (yellow region) is found more on Ta_3N_5 plane around N atoms at the interface. The above result firmly suggests an interfacial charge transfer from $LaTaON_2$ to Ta_3N_5:La and significant increase in carrier concentration on La doped Ta_3N_5 surface. This could be one of the reasons why La-Ta_3N_5 had such high photocurrent.

Facile processes make Ta_3N_5 based photoanodes' probability towards practicality, The PEC performance of the La-Ta_3N_5 compares favorably to those of some representative facilely prepared Ta_3N_5 based photoanodes reported for PEC water oxidation (**Table S1**) [21,25,49–57]. However, further improvement is still needed to develop facile methods to maintain high photocurrent and improve stability.

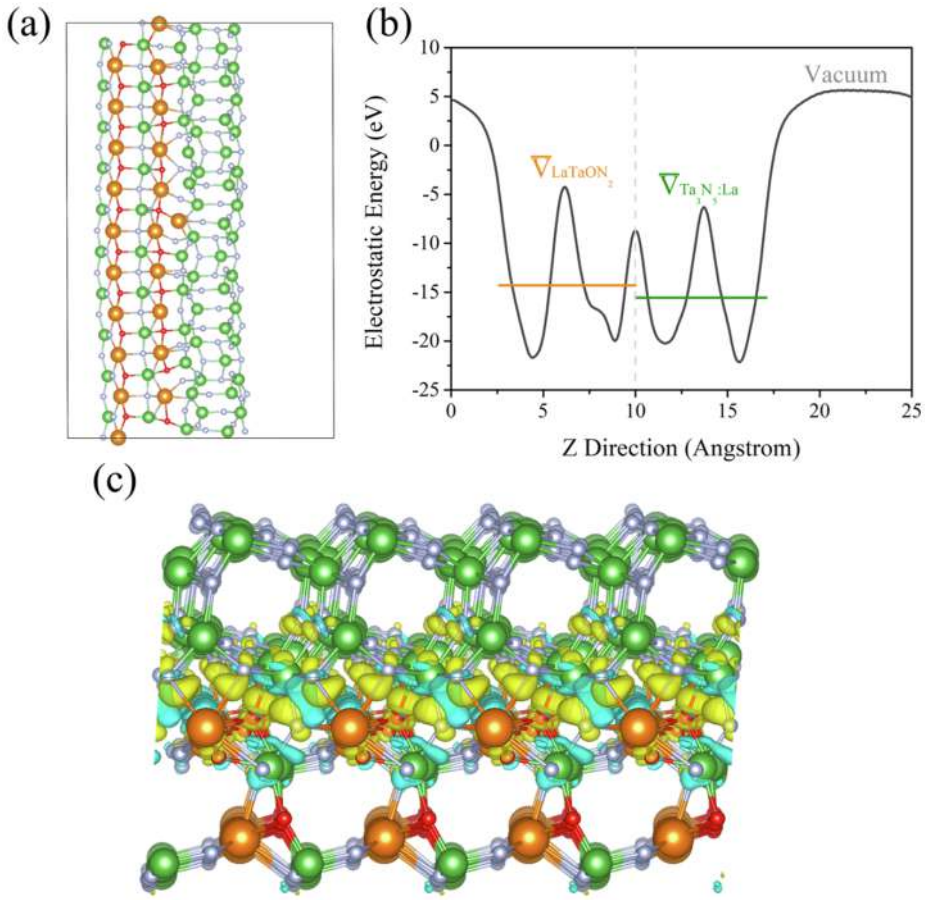

Fig. 8. $LaTaON_2$ (2 0 0)/Ta_3N_5:La (1 1 0) heterostructure, (a) atomic structure, (b) electrostatic potential averaged $\bar{V}$ over the heterostructure, (c) charge density difference of the heterostructure. The yellow and cyan color represent charge accumulation and depletion. The isovalue of the isosurfaces is set to 0.005 electron/bohr^3. La, Ta, O, N atoms are shown in orange, green, red and grey, respectively.

4. Conclusion

Efficient Ta_3N_5 photoanode was fabricated on Ta foil by direct oxidation and nitridation method with $LaCl_3$ flux mediated treatment. Drawing on the experience of previous researchers, surface passivation layer exfoliation and interface subnitride regulation are concurrently achieved. Further loading cocatalyst Co_3O_4 gave a photocurrent of 8.2 mA cm^{-2} at 1.23 V_{RHE} in 1 M NaOH under simulated sunlight (AM 1.5 G, 100 mW cm^{-2}). Through DFT calculation, we reveal that surface doping of La greatly improves its carrier concentration, but due to the localization of La, the effective mass of electrons increases and the mobility decreases, so only trace and surface doping can have a better effect. The heterojunction formed by $LaTaON_2$ and Ta_3N_5:La has a type II structure. The band alignment and charge density difference results show that the heterostructure can effectively separate carriers and further promote the photoelectrochemical performance. To the best of our knowledge, this is the highest photoresponse for Ta_3N_5 prepared by direct oxidation and nitridation of Ta foil. The introduction of $LaCl_3$ flux brings a new look to this traditional method, providing methods for large-area, low-cost, but efficient photoanode.

Declaration of Competing Interest

The authors declare that they have no known competing financial interests or personal relationships that could have appeared to influence the work reported in this paper.

Acknowledgements

This work was supported by National Natural Science Foundation of China (51572239 and 91333203), Program for Innovative Research Team in University of Ministry of Education of China (IRT13037), the National Science and Technology Support Program (2012BAC08B08) and the Major Project of Zhejiang Natural Science Foundation of China (LD18E020002).

Appendix A. Supplementary data

Supplementary data to this article can be found online at https://doi.org/10.1016/j.cej.2020.125161.

References

[1] J. Gong, C. Li, M.R. Wasielewski, Chem. Soc. Rev. 48 (2019) 1862–1864.
[2] Z. Li, W. Luo, M. Zhang, J. Feng, Z. Zou, Energy Environ. Sci. 6 (2013) 347–370.
[3] T. Hisatomi, J. Kubota, K. Domen, Chem. Soc. Rev. 43 (2014) 7520–7535.
[4] C. Zhen, R. Chen, L. Wang, G. Liu, H.-M. Cheng, J. Mater. Chem. A 4 (2016) 2783–2800.
[5] Y. He, James E. Thorne, Cheng, H. Wu, P. Ma, C. Du, Q. Dong, J. Guo, D. Wang, Chem, 1 (2016) 640-655.
[6] M. Xiao, Z. Wang, B. Luo, S. Wang, L. Wang, Appl. Catal. B-Environ. 246 (2019) 195–201.
[7] J. Wang, Y. Jiang, A. Ma, J. Jiang, J. Chen, M. Li, J. Feng, Z. Li, Z. Zou, Appl. Catal. B-Environ. 244 (2019) 502–510.
[8] G. Fu, S. Yan, T. Yu, Z. Zou, Appl. Phys. Lett. 107 (2015) 171902.
[9] M. Xiao, B. Luo, M. Lyu, S. Wang, L. Wang, Adv. Energy Mater. 8 (2018) 1701605.
[10] P. Zhang, T. Wang, J. Zhang, X. Chang, J. Gong, Nanoscale 7 (2015) 13153–13158.

[11] L. Wang, N.T. Nguyen, X. Zhou, I. Hwang, M.S. Killian, P. Schmuki, ChemSusChem 8 (2015) 2615–2620.
[12] L. Wang, X. Zhou, N.T. Nguyen, I. Hwang, P. Schmuki, Adv. Mater. 28 (2016) 2432–2438.
[13] S. Khan, M.J.M. Zapata, D.L. Baptista, R.V. Gonçalves, J.A. Fernandes, J. Dupont, M.J.L. Santos, S.R. Teixeira, J. Phys. Chem. C 119 (2015) 19906–19914.
[14] L. Wang, B. Zhang, Q. Rui, ACS Catal. 8 (2018) 10564–10572.
[15] R. Chen, C. Zhen, Y. Yang, X. Sun, J.T.S. Irvine, L. Wang, G. Liu, H.-M. Cheng, Nano Energy 59 (2019) 683–688.
[16] C. Zhen, L. Wang, G. Liu, G.Q. Lu, H.-M. Cheng, Chem. Commun. 49 (2013) 3019–3021.
[17] M. Zhong, T. Hisatomi, Y. Sasaki, S. Suzuki, K. Teshima, M. Nakabayashi, N. Shibata, H. Nishiyama, M. Katayama, T. Yamada, K. Domen, Angew. Chem. Int. Ed. 56 (2017) 4739–4743.
[18] T. Higashi, H. Nishiyama, Y. Suzuki, Y. Sasaki, T. Hisatomi, M. Katayama, T. Minegishi, K. Seki, T. Yamada, K. Domen, Angew. Chem. Int. Ed. 58 (2019) 2300–2304.
[19] G. Liu, J. Shi, F. Zhang, Z. Chen, J. Han, C. Ding, S. Chen, Z. Wang, H. Han, C. Li, Angew. Chem. Int. Ed. 53 (2014) 7295–7299.
[20] G. Liu, S. Ye, P. Yan, F. Xiong, P. Fu, Z. Wang, Z. Chen, J. Shi, C. Li, Energy Environ. Sci. 9 (2016) 1327–1334.
[21] M. Li, W. Luo, D. Cao, X. Zhao, Z. Li, T. Yu, Z. Zou, Angew. Chem. Int. Ed. 52 (2013) 11016–11020.
[22] B.A. Pinaud, A. Vailionis, T.F. Jaramillo, Chem. Mater. 26 (2014) 1576–1582.
[23] B.A. Pinaud, P.C.K. Vesborg, T.F. Jaramillo, J. Phys. Chem. C 116 (2012) 15918–15924.
[24] Y. Li, L. Zhang, A. Torres-Pardo, J.M. González-Calbet, Y. Ma, P. Oleynikov, O. Terasaki, S. Asahina, M. Shima, D. Cha, L. Zhao, K. Takanabe, J. Kubota, K. Domen, Nat. Commun. 4 (2013) 2566.
[25] E. Nurlaela, M. Nakabayashi, Y. Kobayashi, N. Shibata, T. Yamada, K. Domen, Sustain. Energy Fuels (2020), https://doi.org/10.1039/c9se01319a.
[26] Z.R. Lou, Y.G. Li, L.P. Zhu, W.Y. Xie, W.Z. Niu, H. Song, Z.Z. Ye, S.B. Zhang, J. Mater. Chem. A 5 (2017) 2732–2738.
[27] H. Wang, L. Zhang, Z. Chen, J. Hu, S. Li, Z. Wang, J. Liu, X. Wang, Chem. Soc. Rev. 43 (2014) 5234–5244.
[28] S.J.A. Moniz, S.A. Shevlin, D.J. Martin, Z.-X. Guo, J. Tang, Energy Environ. Sci. 8 (2015) 731–759.
[29] Z. Zou, J. Ye, K. Sayama, H. Arakawa, Nature 414 (2001) 625–627.
[30] Y. Goto, T. Hisatomi, Q. Wang, T. Higashi, K. Ishikiriyama, T. Maeda, Y. Sakata, S. Okunaka, H. Tokudome, M. Katayama, S. Akiyama, H. Nishiyama, Y. Inoue, T. Takewaki, T. Setoyama, T. Minegishi, T. Takata, T. Yamada, K. Domen, Joule 2 (2018) 509–520.
[31] L. Pei, Z. Xu, Z. Shi, H. Zhu, S. Yan, Z. Zou, J. Mater. Chem. A 5 (2017) 20439–20447.
[32] J. Hou, Y. Wu, S. Cao, F. Liang, Z. Lin, Z. Gao, L. Sun, Adv. Energy Mater. 7 (2017) 1700171.
[33] B. Dong, J. Cui, Y. Gao, Y. Qi, F. Zhang, C. Li, Adv. Mater. 31 (2019) 1808185.
[34] Y. Dong, K. He, L. Yin, A. Zhang, Nanotechnology 18 (2007) 435602.
[35] W. Niu, T. Moehl, W. Cui, R. Wick-Joliat, L. Zhu, S.D. Tilley, Adv. Energy Mater. 8 (2018) 1702323.
[36] G. Kresse, D. Joubert, Phys. Rev. B 59 (1999) 1758–1775.
[37] J.P. Perdew, K. Burke, M. Ernzerhof, Phys. Rev. Lett. 77 (1996) 3865–3868.
[38] T. Takata, D. Lu, K. Domen, Cryst. Growth Des. 11 (2011) 33–38.
[39] Z. Wang, Y. Qi, C. Ding, D. Fan, G. Liu, Y. Zhao, C. Li, Chem. Sci. 7 (2016) 4391–4399.
[40] C. Pan, T. Takata, M. Nakabayashi, T. Matsumoto, N. Shibata, Y. Ikuhara, K. Domen, Angew. Chem. Int. Ed. 54 (2015) 2955–2959.
[41] C. Pan, T. Takata, K. Kumamoto, S.S. Khine Ma, K. Ueda, T. Minegishi, M. Nakabayashi, T. Matsumoto, N. Shibata, Y. Ikuhara, K. Domen, J. Mater. Chem. A, 4 (2016) 4544-4552.
[42] J.F. Moulder, W.F. Stickle, P.E. Sobol, P.E. Sobol, Handbook of X-ray Photoelectron Spectroscopy, Perkin-Elmer Corporation, U.S.A., 1992.
[43] W. Niu, L. Zhu, Y. Wang, Z. Lou, Z. Ye, Catal. Sci. Technol. 7 (2017) 1602–1610.
[44] Y. Wang, Z. Lou, W. Niu, Z. Ye, L. Zhu, Nanotechnology 29 (2018) 145402.
[45] L. Sun, Y. Zhuang, Y. Yuan, W. Zhan, X.-J. Wang, X. Han, Y. Zhao, Adv. Energy Mater. 9 (2019) 1902839.
[46] X. An, T. Li, B. Wen, J. Tang, Z. Hu, L.-M. Liu, J. Qu, C.P. Huang, H. Liu, Adv. Energy Mater. 6 (2016) 1502268.
[47] Z. Lou, Y. Li, H. Song, Z. Ye, L. Zhu, RSC Adv. 6 (2016) 45343–45348.
[48] J. Wang, T. Fang, L. Zhang, J. Feng, Z. Li, Z. Zou, J. Catal. 309 (2014) 291–299.
[49] Z. Shi, J. Feng, H. Shan, X. Wang, Z. Xu, H. Huang, Q. Qian, S. Yan, Z. Zou, Appl. Catal.B-Environ. 237 (2018) 665–672.
[50] S.G. Han, S.Y. Chae, S.Y. Lee, B.K. Min, Y.J. Hwang, Phys. Chem. Chem. Phys. 20 (2018) 2865–2871.
[51] Z. Shi, Z. Xu, J. Feng, H. Huang, Q. Qian, S. Yan, Z. Zou, CrystEngComm 20 (2018) 5364–5369.
[52] H. Wang, Z. Shi, S. Yan, Z. Zou, Appl. Phys. Lett. 114 (2019) 132105.
[53] C. Shao, J. Han, G. Liu, Z. Wang, Y. Zhao, X. Zong, C. Li, ChemPhotoChem 2 (2018) 249–256.
[54] S. Suzuki, M. Yanai, T. Yamada, H. Wagata, Y. Sasaki, S. Oishi, K. Domen, K. Teshima, A.C.S. Appl, Energy Mater. 1 (2018) 6129–6135.
[55] T. Fang, H. Huang, J. Feng, Y. Hu, Y. Guo, S. Zhang, Z. Li, Z. Zou, Sci. Bull. 63 (2018) 1404–1410.
[56] H. Hajibabaei, D.J. Little, A. Pandey, D. Wang, Z. Mi, T.W. Hamann, A.C.S. Appl, Mater. Interfaces 11 (2019) 15457–15466.
[57] X. Xiao, M. Iwase, G. Yin, M. Nakabayashi, T. Higashi, N. Shibata, K. Domen, T. Watanabe, ACS Sustainable Chem. Eng. 7 (2019) 19407–19414.